



1 **Disparate evolution mechanisms and optical**
2 **absorption for transboundary soot particles passing**
3 **through inland and sea pathways**

4

5 **Jian Zhang¹, Zexuan Zhang², Keliang Li², Xiyao Chen², Xinpeng Xu², Yangmei**
6 **Zhang³, Anzhou Han⁴, Yuanyuan Wang⁵, Jing Ding¹, Liang Xu⁶, Yinxiao Zhang⁷,**
7 **Hongya Niu⁸, Shoujuan Shu², and Weijun Li^{2,*}**

8

9 ¹School of Environmental and Material Engineering, Yantai University, Yantai 264005,
10 China

11 ²Key Laboratory of Geoscience Big Data and Deep Resource of Zhejiang Province,
12 Department of Atmospheric Sciences, School of Earth Sciences, Zhejiang University,
13 Hangzhou 310027, China

14 ³Key Laboratory of Atmospheric Chemistry, China Meteorological Administration,
15 Beijing 100081, China

16 ⁴Trier College of Sustainable Technology, Yantai University, Yantai 264005, China

17 ⁵Hangzhou International Innovation Institute of Beihang University, Hangzhou 310000,
18 China

19 ⁶College of Sciences, China Jiliang University, Hangzhou 310018, China

20 ⁷Flight College, Shandong University of Aeronautics, Binzhou 256600, China

21 ⁸Key Laboratory of Resource Exploration Research of Hebei Province, Hebei
22 University of Engineering, Handan 056038, China

23 *Corresponding Email: liweijun@zju.edu.cn (W. J. Li)



24 **Abstract**

25 Soot particles, as a type of warming aerosols, play a critical role in climate warming.
26 During transport, these particles undergo atmospheric condition-dependent aging
27 processes that influence their microphysical and optical properties. Here, we
28 investigated the variations in morphology, mixing states, sizes, and optical absorption
29 of soot-containing particles and further revealed their evolution mechanisms during two
30 distinct transboundary transport through the inland and sea pathways. Comparing
31 transboundary soot-containing particles transported through the inland and sea
32 pathways, we found more soot cores in the latter individual particles, although their
33 dominant mixing states exhibited a similar transition from partly-coated at 62-67% by
34 number to embedded structures at 71-72%. The core-shell size ratio (D_p/D_c) and soot
35 core fractal dimension of embedded soot-containing particles transported through the
36 sea pathway were both greater compared to the inland pathway. These differences were
37 attributed to distinct evolution mechanisms experienced by soot-containing particles
38 during transport: heterogeneous aging processes through the inland pathway and cloud
39 processes through the sea pathway. Optical simulation showed amplified light
40 absorption of soot-containing particles during their transboundary transport.
41 Furthermore, the radiative absorption amplification per unit D_p/D_c change reduced by
42 72% due to the entrainment of multiple soot cores within individual particles following
43 the transport pathway change from the inland to the sea. This study suggests varied
44 mixing configurations and radiative absorption of transboundary soot-containing
45 particles driven by different environmental conditions and highlights the necessity of
46 incorporating multicore black carbon mixing structures into climate models.



1. Introduction

In recent years, eastern China still faces severe haze pollution in winter despite a series of control policies adopted by the local government (Peng et al., 2021; Zang et al., 2022; Zhai et al., 2021). High concentrations of fine haze particles not only affect human health (Geng et al., 2021; Zhang et al., 2017b), but also influence the global climate (Li et al., 2016a; Suzuki and Takemura, 2019). In addition to high emissions of pollutants and stable meteorological conditions (Niu et al., 2016; Zhao et al., 2019; Zheng et al., 2015), transboundary transport of pollutants has been confirmed to be an important factor causing the formation of regional haze pollution in eastern China in winter (Li et al., 2019; Zhang et al., 2021; Zhang et al., 2019a). For example, large amounts of haze pollutants in the North China Plain (NCP) can be transported thousands of kilometers to the Yangtze River Delta (YRD) under cold fronts to induce long-lasting regional haze events (Huang et al., 2020).

In eastern China, the NCP and the YRD as two rapid economic developed regions suffer the heaviest haze pollution (Zhong et al., 2019). Recent studies found frequent transboundary transport of pollutants from the NCP to the YRD using various methods including field observation and model simulation (Kang et al., 2019; Li et al., 2019; Xie et al., 2023; Yan et al., 2024; Zhang et al., 2021). For instance, Kang et al. (2019) utilized numerical models to show that the PM_{2.5} contribution from the NCP reached to ~30% in the YRD under cold fronts. Field results showed that concentrations of organic matter and secondary inorganic ions in PM_{2.5} in the YRD increased by approximately 1-2 times following the invasion of haze pollutants from the NCP (Zhang et al., 2021). Xie et al. (2023) also suggested that carbonaceous aerosols and secondary inorganic ions were effectively transported from the NCP to the YRD based on the simulation of the average atmospheric age of haze particles. During the transboundary transport, abundant secondary aerosols (e.g., sulfate and nitrate) can be formed through heterogeneous chemical processes, influencing the particulate hygroscopicity (Li et al., 2019; Li et al., 2025; Zhang et al., 2021). Although these studies revealed changes in the bulk chemical composition of fine particles and main formation processes of



76 secondary aerosols during the transport, there is a lack of evolution mechanisms of
77 transboundary particles and their potential health or climate effects.

78 We noticed that cold fronts had different pathways to convey air pollutants from
79 the NCP to the YRD depending on the location of high-pressure systems. The previous
80 studies showed that cold fronts from the high-pressure system locating in the west of
81 the NCP normally transported haze pollutants across city clusters in eastern China (Hou
82 et al., 2020; Jin et al., 2021). If the high-pressure system located in the interior of the
83 NCP, heavy haze covering the Jing-Jin-Ji region (i.e., Beijing, Tianjin, and Hebei) could
84 move out from inland China to the East China Sea and return into the inland region
85 under prevailing winds, influencing air quality of the YRD (see section 3.1). These haze
86 movements from the NCP to the YRD were clearly observed from the satellites
87 (<https://worldview.earthdata.nasa.gov>). To our knowledge, the previous studies only
88 focused on the haze transportation from the NCP to the YRD through the inland
89 pathway based on field measurements and model simulation (Huang et al., 2020; Yan
90 et al., 2024). Obviously, there was a bench of data available from national ground
91 monitoring net station of air quality to support the measurements and modelling studies.
92 However, transboundary haze pollutants crossed the East China Sea remain unexplored.
93 We expect different chemical mechanisms and aging processes in gas-aerosol
94 interactions in two haze layers because of different meteorological factors (e.g., relative
95 humidity) and pollutant emissions in transport pathways.

96 Soot particles (i.e., black carbon, also called elemental carbon) emitted from
97 incomplete burning of fossil fuels and biomass are important light absorbing aerosols
98 in fine particles, exerting favorable effects on global warming in the atmosphere (Bond
99 et al., 2013; Cappa et al., 2012; Jacobson, 2001). Soot particles serve as an excellent
100 tracer to reflect atmospheric aging because their morphology (Fierce et al., 2020; Wu
101 et al., 2018; Yuan et al., 2019), mixing states (Wang et al., 2019; Wang et al., 2016),
102 sizes (Adachi et al., 2014; Xu et al., 2020), and mass (Liu et al., 2020; Zhang et al.,
103 2018) can be significantly altered during transport. Previous global studies examining
104 pollutant transport, such as trans-oceanic dust events affecting East Asia (Xu et al., 2020)



105 and North America outflow influencing the Azores in the North Atlantic (China et al.,
106 2015), have extensively utilized soot particles as a primary investigative target to
107 understand environmental impacts. The transport corridor from the NCP to the YRD
108 represents no exception, where soot particles persist as a critical, abundant component
109 of atmospheric aerosols (Huang et al., 2020; Zhang et al., 2023). Compared to transport
110 over inland China, soot particles transported to the YRD from the NCP via the East
111 China Sea may encounter more humid conditions. These distinct atmospheric
112 environments can lead to different alterations in soot physicochemical properties (Li et
113 al., 2024). Therefore, the evolution of soot particles and their environmental and climate
114 impacts should be examined in different synoptic weather processes. Although
115 simulating soot climate effect is readily achievable in models, these simulations often
116 overlook alterations in soot microphysical properties due to limited studies, thereby
117 introducing considerable uncertainties into the results (IPCC, 2021).

118 To bridge this critical gap, we observed two types of transboundary transport
119 events of haze pollutants (passing through the inland and through the sea pathways)
120 from the NCP to the YRD and first compared physicochemical characteristics (e.g.,
121 morphology, mixing states, and sizes) of transboundary soot particles in the two events
122 by various microscopic measurements. Based on microscopic observations, the
123 evolution mechanisms of two types of transboundary soot particles were unveiled.
124 Using a novel optical calculation model, we further estimated the change in soot optical
125 absorption between two types of transboundary transport. This study aims to emphasize
126 how divergent transport environments (inland vs. sea) impart distinct physicochemical
127 effects on soot particles. This promotes understanding of the weather-aerosol-pollution-
128 climate nexus, ultimately informing more accurate prediction of soot role in regional
129 climate forcing and atmospheric chemistry.

130

131 **2. Methods**

132 **2.1 Sample collection**

133 Three sites (Beijing, Handan, and Zhengzhou) in the NCP and two sites (Nanjing



134 and Hangzhou) in the YRD were selected to collect ambient PM_{2.5} and individual
135 aerosol particles in December 2017 and 2020 based on the transport behavior of
136 airborne pollutants under cold fronts in winter (Figure S1). Beijing, Handan, and
137 Zhengzhou are located in the northern, central, and southern parts of the NCP,
138 respectively. Beijing is a typical megacity and influenced by local emissions and
139 regional transport, while Handan and Zhengzhou are two typical industrial cities and
140 affected by local industrial, vehicular, and residential emissions. Nanjing and Hangzhou
141 are two megacities located in the northern and southern parts of the YRD. These two
142 megacities can be influenced when haze particles in the NCP invade the YRD.
143 Therefore, the above five cities in the NCP and YRD are representative for exploring
144 transboundary transport of aerosols (e.g., soot particles) in haze plumes. The detailed
145 information of the sampling sites has been described in previous studies (Zhang et al.,
146 2023; Zhang et al., 2021).

147 Ambient PM_{2.5} and blank samples (no pumping) were collected on preheated
148 quartz filters with 90 mm diameters (600°C for 4 hr, Whatman) twice a day from 8:30
149 (local time) to 20:00 and from 20:30 to 8:00 the next day using medium volume
150 samplers (TH-16A, Wuhan Tianhong, 100 L min⁻¹). Individual aerosol particles were
151 sampled on transmission electron microscopy (TEM) grids and silicon wafers four
152 times a day at around 2:00 (local time), 9:00, 14:00, and 20:00 utilizing individual
153 particle samplers (DKL-2, Genstar, 1 L min⁻¹) equipped with a 0.5 mm jet nozzle
154 impactor. To avoid particles overlapping on the substrate, the sampling duration of
155 individual particles needs to be adjusted from 30 s to 15 min according to current PM_{2.5}
156 concentrations. Hourly PM_{2.5} concentrations and meteorological parameters including
157 relative humidity (RH) and winds were derived from local monitoring stations
158 (<https://www.aqistudy.cn/>).

159

160 **2.2 PM_{2.5} and individual particle analyses**

161 Water-soluble inorganic ions (i.e., NO₃⁻, SO₄²⁻, NH₄⁺, F⁻, Cl⁻, Na⁺, K⁺, Ca²⁺, and
162 Mg²⁺), carbonaceous components (organic and elemental carbon), and trace metallic



elements in PM_{2.5} samples were analyzed using an ion chromatography system (Dionex ICs-90, USA), an OC/EC analyzer (Sunset Laboratory, USA), and inductively coupled plasma mass spectrometry (ICP-MS, Agilent 7500ce). The detailed experimental processes can be found in previous studies (Pan et al., 2013; Zhang et al., 2017a). In this study, organic matter (OM) concentrations were obtained by multiplying organic carbon (OC) concentrations by 1.91 reported by Xing et al. (2013).

Morphology, mixing states, and compositions of individual aerosol particles collected on TEM grids were examined by TEM equipped with energy-dispersive X-ray spectrometry (EDS) (JEM-2100, JEOL). The acquisition time of TEM images and EDS spectra is usually controlled within 15 s because of the damage of electron beams to non-refractory aerosols. To better observe soot mixing states and measure soot geometrical parameters, we enhanced the electron beam to sublime non-refractory coatings of indiscernible soot cores after conventional TEM observations. Copper element was excluded from particle EDS spectra because TEM grids are made of copper (Li et al., 2025). Using an image analysis software (Radius, EMSIS GmbH), we further obtained the equivalent circle diameter (ECD), length, and area of particles in TEM images. In this work, 3642 individual particles were analyzed by TEM in total.

Three-dimensional morphology of individual particles collected on silicon wafers was probed by atomic force microscopy (AFM, Dimension Icon) in tapping mode. Employing a professional image analysis software (NanoScope Analysis), the bearing area (A) and the bearing volume (V) of particles in AFM images were quantified. The ECD and the equivalent sphere diameter (ESD) of these particles can be calculated applying equations (1) and (2).

$$ECD = \sqrt{\frac{4A}{\pi}} \quad (1)$$

$$ESD = \sqrt[3]{\frac{6V}{\pi}} \quad (2)$$

Figure S2 shows that there is a good correlation between the ESD and the ECD with slopes at 0.62 for passing through the inland pathway transport and 0.39 for



188 passing through the sea pathway transport. According to the relationship between the
189 ESD and the ECD, ESDs of particles observed by TEM were computed. The ESDs of
190 soot particles were perceived as equivalent to their ECDs because they are composed
191 of solid carbonaceous spheres that are not affected by substrates in terms of morphology
192 (Barone et al., 2012; Li et al., 2016b).

193 The size ratio of soot-containing particles to their soot cores (D_p/D_c) was evaluated
194 using equation (3):

$$D_p/D_c = \frac{ESD_{\text{soot-containing}}}{ESD_{\text{soot}}} \quad (3)$$

195 where $ESD_{\text{soot-containing}}$ is the ESD of soot cores with their coatings and ESD_{soot} is the
196 soot core ESD.

197 Based on the scaling law in following equations, we obtained the fractal dimension
198 (D_f) of soot particles, which can be used to reflect the compactness of soot particles:

$$N = k_g \left(\frac{2R_g}{d_p} \right)^{D_f} \quad (4)$$

$$N = k_a \left(\frac{A_a}{A_p} \right)^\alpha \quad (5)$$

$$\delta = \frac{2a}{l} \quad (6)$$

$$\frac{L_{\max}}{2R_g} = 1.50 \pm 0.05 \quad (7)$$

199 where N is the monomer number in soot particles, k_g is the fractal prefactor, R_g is the
200 gyration radius of soot particles, d_p is the average diameter of soot monomers, A_a is the
201 projected area of soot particles, A_p is the average projected area of soot monomers, k_a
202 is a constant, α is an empirical projected area exponent, δ is the overlap parameter of
203 soot monomers, a is the average radius of adjacent soot monomers, l is the spacing of
204 adjacent soot monomers, and L_{\max} is the maximum length of soot particles. k_a and α
205 depend on δ (Oh and Sorensen, 1997).

206

207 2.3 Meteorological fields and geographic sources

208 Wind fields coupled with surface $PM_{2.5}$ concentrations covering eastern China



209 were obtained from European Centre for Medium-Range Weather Forecasts (ECMWF,
210 <https://earth.nullschool.net/>). Meteorological fields including winds and relative
211 humidity (RH) in eastern China at 1000 hPa were simulated using $1^\circ \times 1^\circ$ Final
212 Reanalysis Data (FNL) from the National Centers for Environmental Prediction (NCEP,
213 <https://rda.ucar.edu/datasets/ds083.2/>).

214 The potential geographic sources of PM_{2.5} at observation sites (Nanjing and
215 Hangzhou) in the YRD were identified based on the concentration-weighted trajectory
216 (CWT) analysis. In this study, 72 hr of air mass backward trajectories simulated from
217 the wind data sets in the Nation Oceanic Atmospheric Administration (NOAA,
218 <ftp://arlftp.arlhq.noaa.gov/pub/archives/gdas1>) were used for the CWT analysis. The
219 resolution of CWT trajectories consists of thousands of grid cells is $0.3^\circ \times 0.3^\circ$. The
220 equation for the CWT analysis is as follows:

$$C_{ij} = \frac{1}{\sum_{k=1}^N \tau_{ijk}} \sum_{k=1}^N C_k \tau_{ijk} \quad (8)$$

221 where C_{ij} is the average PM_{2.5} concentration in a grid cell (i, j); C_k is the measured PM_{2.5}
222 concentration for the trajectory k arriving at the observation site; τ_{ijk} is the number of
223 trajectory endpoints in the grid cell (i, j) for the C_k sample; N is the number of samples
224 with trajectory endpoints in the grid cell (i, j).

225 In the CWT analysis, a weighing function as shown in equation (9) was applied to
226 further improve the CWT accuracy:

$$W = \begin{cases} 1 & \text{for } \log(n+1) \geq 0.85 \times \max_{\log(n+1)} \\ 0.725 & \text{for } 0.6 \times \max_{\log(n+1)} \leq \log(n+1) < 0.85 \times \max_{\log(n+1)} \\ 0.475 & \text{for } 0.35 \times \max_{\log(n+1)} \leq \log(n+1) < 0.6 \times \max_{\log(n+1)} \\ 0.175 & \text{for } \log(n+1) < 0.35 \times \max_{\log(n+1)} \end{cases} \quad (9)$$

227 where $\log(n+1)$ is the density of trajectories.

228

229 2.4 Optical calculation

230 The Electron-Microscope-to-BC-Simulation (EMBS) tool developed by Wang et
231 al. (2021) was used to model morphology and mixing states of soot particles. The
232 EMBS tool capable of building various soot-containing particle models can be applied



233 in DDSCAT 7.3 to calculate soot optical properties based on the discrete dipole
234 approximation (DDA). DDA is completely flexible to the geometry of object particles
235 under the condition that the inter dipole separation d follows $|m|kd < 0.5$ and $k = 2\pi/\lambda$,
236 where m is the refractive index of particles and λ is the incident light wavelength. To
237 minimize DDA uncertainty, the dipole size is much smaller than the soot monomer size.
238 Based on sizes and mixing states of soot-containing particles as well as D_f and numbers
239 of soot cores obtained from microscopic analyses, we employed EMBS and DDSCAT
240 7.3 to calculate the light absorption enhancement (E_{abs}) of soot-containing particles
241 relative to their soot cores at 550 nm λ . In this study, soot-containing particles with one,
242 two, and three or more soot cores were distinguished. The volumes of soot cores and
243 their coatings remained constant in the optical calculation. The refractive indices of soot
244 cores and coatings were considered as $1.85 + 0.71i$ (Bond and Bergstrom, 2006) and
245 $1.53 + 0i$ (Worringen et al., 2008), respectively. Details about the EMBS and DDSCAT
246 7.3 can be found in the previous study (Wang et al., 2021).

247

248 **3. Results and discussion**

249 **3.1 Determination of two types of transport models**

250 Figures S3a-b show variations in hourly winds and $PM_{2.5}$ concentrations at the
251 observation sites in the NCP and the YRD from December 28 to 31, 2017 and from
252 December 5 to 8, 2020. The prevailing wind significantly changed from weak southern
253 winds to strong northern winds in the NCP and the YRD on December 30, 2017 and
254 December 7, 2020 under cold fronts (Figures S3a-b). On the same day, the average
255 $PM_{2.5}$ concentration in the NCP rapidly decreased from $318 \mu g m^{-3}$ during the first
256 observation period and $179 \mu g m^{-3}$ during the second observation period to $33 \mu g m^{-3}$
257 and $37 \mu g m^{-3}$ (Figures S3a-b). After 6-9 hours, the average $PM_{2.5}$ concentration in the
258 YRD suddenly increased from $62 \mu g m^{-3}$ during the first observation period and $51 \mu g$
259 m^{-3} during the second observation period to $308 \mu g m^{-3}$ and $113 \mu g m^{-3}$ (Figures S3a-
260 b). Similar changes in $PM_{2.5}$ concentrations accompanied by winds were also found in
261 many transboundary transport events of pollutants (Wu et al., 2022; Xie et al., 2023;



262 Yan et al., 2024; Zhao et al., 2021). As a result, we inferred that there was a typical
263 transboundary transport process of pollutants from the NCP to the YRD on December
264 30-31, 2017 and December 7-8, 2020, respectively.

265 Figure 1 displays meteorological fields coupled with surface PM_{2.5} concentrations
266 in eastern China during two transboundary transport events of pollutants. In the first
267 transport event, the wind blew from the NCP through the inland pathway towards the
268 YRD under the high-pressure system located in the west of the NCP (Figures 1a, 1c,
269 and S3c). It is interesting that there was a significant change in the wind field following
270 the high-pressure system movement to the interior of the NCP during the second
271 transport event compared to the first event, manifested as the wind mainly blowing from
272 the NCP to the East China Sea and then to the YRD (Figures 1b, 1d, and S3d). Although
273 a previous study also discovered comparable wind fields between the NCP and the YRD
274 using a weather model, the changes in chemical compositions and microphysical
275 properties of haze particles have not been defined during the transboundary transport
276 (Wu et al., 2022). To determine whether the transport pathway of pollutants was
277 consistent with the wind field, the PM_{2.5} transport pathway was simulated based on the
278 CWT analysis (Figure 2). Figure 2 shows that PM_{2.5} in Nanjing and Hangzhou was
279 mainly transported from the NCP through the inland pathway during the first transport
280 event but through the sea pathway during the second transport event. Therefore, we
281 concluded two transport models of haze pollutants from the NCP to the YRD, namely
282 passing through the inland and through the sea pathways.

283 During two transboundary transport events, concentrations of chemical
284 compositions in PM_{2.5} in the NCP and the YRD significantly changed (Figure S4). The
285 concentration of secondary inorganic ions in the NCP decreased from 92-126 $\mu\text{g m}^{-3}$
286 during the polluted period to 28-30 $\mu\text{g m}^{-3}$ during the clean period (Figure S4). OM and
287 EC concentrations in the NCP also decreased from 43-76 $\mu\text{g m}^{-3}$ and 1.5-2.1 $\mu\text{g m}^{-3}$
288 during the polluted period to 17-31 $\mu\text{g m}^{-3}$ and 0.7-0.9 $\mu\text{g m}^{-3}$ during the clean period
289 (Figure S4). Following the transportation of large amounts of pollutants from the NCP
290 to the YRD, the concentrations of secondary inorganic ions, OM, and EC in the YRD



291 increased from 28-37 $\mu\text{g m}^{-3}$, 13-19 $\mu\text{g m}^{-3}$, and 1.0-1.4 $\mu\text{g m}^{-3}$ during the clean period
292 to 63-65 $\mu\text{g m}^{-3}$, 32-36 $\mu\text{g m}^{-3}$, and 1.6-2.7 $\mu\text{g m}^{-3}$ during the polluted period,
293 respectively (Figure S4). These results suggest that massive primary and secondary
294 aerosols including EC (i.e., soot) were transported from the NCP to the YRD under cold
295 fronts, both through the inland and the sea pathways.

296 Based on simulated meteorological fields, we noticed that polluted air masses
297 passing through the sea pathway underwent wetter environment during transboundary
298 transport compared to that passing through the inland pathway (Figures 1c-d). Table S1
299 also shows much higher average RH at 90% in the YRD following the transport of haze
300 pollutants from the NCP to the YRD through the sea pathway in contrast to the inland
301 pathway (RH = 83%). High RH can contribute to the transformation of microphysical
302 properties (e.g., mixing states, sizes, and morphology) of soot particles in the
303 atmosphere, but the reaction mechanism may vary under different high RH levels (Fu
304 et al., 2022; Zhang et al., 2023). Consequently, we further investigated and compared
305 the microscopic characteristics of soot particles during their transboundary transport
306 through the inland and through the sea pathways.

307

308 **3.2 Classification and fraction change of soot particles: inland vs. sea**

309 Based on morphology, components, and mixing states of individual transported
310 particles examined by TEM-EDS, they were classified into soot-containing, S-
311 OM/metal/fly ash/mineral, S-rich, and OM/metal/fly ash/mineral particles (Figure S5).
312 The specific classification criteria were described in Text S1. Figure S5 shows that the
313 number fraction of soot-containing particles in the NCP decreased from 45% and 51%
314 during the polluted period to 13% and 18% during the clean period following
315 transboundary transport of haze plumes through the inland and the sea pathways. When
316 large amounts of haze pollutants were transported into the YRD from the NCP through
317 the inland and the sea pathways, the number fraction of soot-containing particles in the
318 YRD increased from 38% and 34% during the clean period to 53% and 65% during the
319 polluted period (Figure S5). The change in the number fraction of soot-containing



320 particles in the NCP and the YRD during transboundary transport is consistent with the
321 variation of EC concentrations. These results suggest that abundant soot-containing
322 particles in the NCP were transported to the YRD following transboundary transport of
323 haze plumes.

324 The morphology and mixing states of soot particles can be changed during
325 transport due to atmospheric aging (Li et al., 2024). Figure 3 shows morphology of soot
326 particles and their mixing structures with other aerosol components observed by TEM.
327 Based on the mixing structure of soot particles, they were divided into three categories:
328 bare-like, partly-coated, and embedded soot particles (Figure 3). Bare-like soot
329 particles are characterized by being isolated and externally mixed with other aerosols
330 (Figure 3a). Partly-coated soot particles manifest as a portion of them being coated by
331 other aerosol components (Figure 3b). Embedded soot particles mean they are
332 completely enveloped by other aerosol materials (Figure 3c). Among these three types
333 of soot particles, bare-like soot particles were considered to be more freshly emitted,
334 while embedded soot particles were more aged (China et al., 2015). To observe
335 embedded soot particles more clearly, their non-refractory coatings (e.g., S-rich
336 particles) were sublimed under stronger electron beam (Figure 3c). In some individual
337 soot-containing particles, thin halos around aerosol components were observed (Figure
338 3c). These thin halos have been confirmed to be water rims left by the dehydrating of
339 aqueous particles because their EDS spectra are similar to the substrate but different
340 from the organic coating (Zhang et al., 2023). Therefore, soot aggregates with water
341 rims were identified as a type of embedded soot particles.

342 TEM observations showed that there were different numbers of soot cores in
343 individual soot-containing particles during transboundary transport (Figure 4a). Based
344 on the number of soot cores in individual soot-containing particles, we further divided
345 partly-coated soot-containing particles and embedded soot-containing particles into
346 them with 1 soot core, 2 soot cores, and ≥ 3 soot cores (Figure 4a). Figures 4b-c show
347 the variation in the number fraction of soot-containing particles with different mixing
348 structures and soot core numbers during transboundary transport through the inland and



349 the sea pathways. During the polluted period, partly-coated types were dominant in
350 soot-containing particles in the NCP, accounting for 62-67% (Figures 4b-c). Following
351 the transboundary transport of haze plumes through the inland pathway, the dominated
352 soot-containing particles changed from partly-coated at 67% by number in the NCP to
353 embedded types at 71% in the YRD (Figure 4b). Meanwhile, more than 75% of them
354 had one soot core (Figure 4b). However, we noticed that the soot core number in the
355 dominated soot-containing particles increased from 1 in the NCP to ≥ 3 in the YRD in
356 addition to the change in the dominated mixing structures from partly-coated at 62%
357 by number to embedded ones at 72% when plentiful soot-containing particles were
358 transported through the sea pathway (Figure 4c). These results indicate that soot-
359 containing particles may be subject to different aging processes during their
360 transboundary transport through the inland and the sea pathways. Moreover, large
361 numbers of soot-containing particles with multiple soot aggregates were also observed
362 in an aged atmospheric environment (Wu et al., 2016). However, their aging
363 mechanisms were not effectively elucidated. The potential aging mechanisms for soot-
364 containing particles in two transboundary transport events are discussed in the
365 following section.

366

367 **3.3 Variation in microphysical characteristics of soot particles and potential aging** 368 **mechanisms: inland vs. sea**

369 Figure 5 shows number percentages of bare-like, partly-coated, and embedded
370 soot-containing particles with different numbers of soot cores in different size bins in
371 the NCP and the YRD during two transboundary transport events. Figure 6 displays
372 size distributions of partly-coated and embedded soot-containing particles during their
373 transboundary transport. Bare-like soot particles were mainly concentrated in the finer
374 size range of 0-200 nm during the transboundary transport (Figure 5). In the NCP,
375 partly-coated soot-containing particles with 1 soot core dominated soot-containing
376 particles and mainly distributed in the size range of 200-500 nm during the polluted
377 period (Figures 4b, c and 5a, c). Figure 6a, c shows consistent results that the size



378 distribution of partly-coated soot-containing particles in the NCP had a peak at 396 nm
379 for the transportation through the inland pathway and at 384 nm for the transportation
380 through the sea pathway. As embedded soot-containing particles became the dominant
381 type during the transboundary transport, their size distribution presented a peak at a
382 larger diameter of 505 nm (inland) and at a much larger diameter of 925 nm (sea)
383 compared to the former diameters at 464 nm and 446 nm (Figure 6). Meanwhile, the
384 preponderant soot-containing particles in the YRD, i.e., embedded ones with 1 core
385 (inland) and ≥ 3 cores (sea), dominated in the coarser size range of 500-700 nm and in
386 the much coarser size range of > 1600 nm, respectively (Figure 5b, d). These findings
387 suggest that aging processes of soot-containing particles during the transboundary
388 transport through the sea pathway not only acquired more soot cores but also greatly
389 enlarged their sizes in contrast to the inland pathway. Consistently, high numbers of
390 soot cores were found in coarse particles of ≥ 800 nm during transboundary transport
391 of biomass burning emissions (Chen et al., 2023).

392 The D_p/D_c ratio of transboundary soot-containing particles was calculated to
393 reflect the coating thickness of soot particles and to quantify the aging degree of soot
394 particles (Figure 7). During two transboundary transport events, the mean D_p/D_c ratios
395 of partly-coated and embedded soot-containing particles presented similar levels at
396 2.37-2.41 and 2.85-2.92 in the NCP (Figure 7). Following the transboundary transport
397 of soot-containing particles through the inland pathway, the mean D_p/D_c ratios of partly-
398 coated and embedded soot-containing particles increased from 2.37 and 2.85 in the NCP
399 to 2.79 and 3.41 in the YRD (Figure 7a). This amount of increase for the D_p/D_c ratio of
400 soot-containing particles is comparable to that from ~ 1.8 to ~ 2.2 during haze evolution
401 (Zhang et al., 2019b) and from 1.42 to 1.78 during dust storm transport (Xu et al., 2020).
402 Moreover, consistent with these studies, we observed a transition in the dominant
403 mixing state of soot particles with secondary coatings from partly-coated with single
404 soot core to embedded with single soot core configurations during the transboundary
405 transport through the inland pathway (Figure 4b), indicating that coagulation played a
406 negligible role in the aging process (China et al., 2015). Soot particles have been



demonstrated to promote the formation of secondary aerosols around them via heterogeneous or aqueous-phase reactions (Farley et al., 2023; Han et al., 2013; Zhu et al., 2025). Figure 8 displays mixing structures of soot-containing particles when they invaded into the YRD through the inland and the sea pathways. It is noted that water rims around soot-containing particles transported through the inland pathway were not observed (Figure 8a, c-d). This implies that aqueous-phase chemistry contributed minimally to secondary aerosol formation on soot particles during the transboundary transport through the inland pathway. As a result, heterogeneous aging processes might mainly drive the enhancement of secondary aerosols on soot-containing particles transported through the inland pathway and enlarged their D_p/D_c ratios. When soot-containing particles were transported from the NCP to the YRD through the sea pathway, the partly-coated D_p/D_c ratio slightly increased from 2.41 to 2.66, but the embedded D_p/D_c ratio largely increased from 2.92 to 4.38 (Figure 7b). Similar results were also found in cloud processes with the D_p/D_c increase from 2.3 to 4.4 for embedded soot-containing particles reported by Fu et al. (2022). Moreover, Xu et al. (2020) showed a relatively high D_p/D_c increase proportion of soot-containing particles at ~40% during the transportation of dust storms from China across the East China Sea with humid air to Japan. Based on observed and simulated RH in eastern China (Table S1 and Figures 1c-d), soot-containing particles could experience wetter environments with > 90% RH during transboundary transport through the sea pathway compared with the inland pathway. We indeed observed obvious water rims around soot-containing particles transported through the sea pathway compared to the inland pathway (Figure 8). The presence of water rims indicates that those soot-containing particles were in the aqueous phase prior to being analyzed by TEM (Zhang et al., 2023). Liu et al. (2018) also revealed pronounced aqueous-phase signatures surrounding cloud droplet residuals, as indicated by water rims. AFM measurements further confirmed that the particles transported through the sea pathway exhibited a droplet morphology (Figure S2b). Moreover, the observed phenomenon of two or more soot cores within individual particles transported through the sea pathway aligns with the findings that a single cloud



436 droplet can entrain numerous refractory aerosol particles (e.g., soot) (Ding et al., 2025;
437 Liu et al., 2018). Therefore, soot-containing particles predominantly underwent cloud
438 process aging under extremely high RH of > 90% conditions during the transboundary
439 transport through the sea pathway, resulting in a significant thickening of coatings on
440 soot cores.

441 The D_f of soot particles serves as a critical metric for assessing their compactness
442 and degree of atmospheric aging processes, providing a quantitative basis for black
443 carbon characterization (Li et al., 2024; Pang et al., 2022). Figure 9 presents the
444 evolution of D_f for partly-coated and embedded soot particles during atmospheric
445 transport through the inland and sea pathways. The D_f of partly-coated and embedded
446 soot particles increased from 1.81 and 1.90 in the NCP to 1.84 and 1.93 in the YRD
447 following the transboundary transport through the inland pathway (Figures 9a-b),
448 suggesting that secondary coatings formed via heterogeneous aging processes enhanced
449 soot compactness during the transport. This varied result of soot D_f during the
450 transboundary transport through the inland pathway is similar to that during the
451 dynamic progression of regional heavy haze pollution in winter (Zhang et al., 2023).
452 However, when soot particles were transported to the YRD from the NCP through the
453 sea pathway, their D_f increased from 1.81 for partly-coated soot and 1.89 for embedded
454 soot to 1.85 and 2.07 (Figures 9c-d). This suggests that the structural collapse of
455 embedded soot particles was more pronounced compared to partly-coated soot particles
456 during the transport through the sea pathway. Moreover, in contrast to the inland
457 pathway, the D_f of embedded soot particles transported through the sea pathway showed
458 a 9.5% greater amplitude (Figure 9). This comparative result is consistent with the
459 observed differences in the D_p/D_c of soot-containing particles during two distinct
460 atmospheric transport events (Figure 7), indicating that cloud process aging under
461 extremely high RH of > 90% can greatly promote the structural collapse of soot
462 aggregates. This mechanism can be ascribed to surface tension induced by the
463 hygroscopic growth of secondary coatings on soot under elevated RH, which collapse
464 the soot fractal morphology through water-mediated structural restructuring (Schnitzler



et al., 2017). Therefore, cloud process aging of soot-containing particles during the transboundary transport through the sea pathway acted synergistically to (1) facilitate the entrainment of multiple soot cores, (2) substantially enhance their D_p/D_c ratios by ~50%, and (3) induce more pronounced collapse of soot fractal structures with D_f from 1.89 to 2.07.

3.4 Optical absorption of soot particles: inland vs. sea

Based on mixing states of soot particles during the transboundary transport, the light absorption enhancement (E_{abs}) of soot-containing particles with 1-3 cores and different mixing structures (partly-coated and embedded configurations) was calculated by the DDA combined with the EMBS. Considering that embedded soot cores were often distributed at the periphery rather than the center within individual particles (Figure 8), we conducted optical simulations of embedded soot-containing particles based on this realistic mixing structure. In the optical calculation, the diameters of single soot cores and coatings were presumed to 194 nm and 925 nm according to their size distribution (Figures S6 and 6d), and the total volume of soot cores in individual constructed particles was constant when their numbers were changed.

Figure 10a shows the change in the E_{abs} of soot-containing particles following their aging from partly-coated to embedded states. The E_{abs} of soot-containing particles with one soot core increased from 1.80 for the partly-coated structure to 2.83 for the embedded structure (Figure 10a). When soot-containing particles had two soot cores, the E_{abs} increased from 1.74 to 2.44, representing a 0.4-fold increase, with soot aging from partly-coated to embedded configurations (Figure 10a). Following the soot core number increase to three, the E_{abs} of soot-containing particles increased by 117% (from 1.04 to 2.26) when their mixing structures changed from partly-coated to embedded status (Figure 10a). These results suggest that individual particles containing higher numbers of soot cores demonstrate larger optical absorption amplification during atmospheric aging processes although their E_{abs} values were lower. Previous studies also found lower absorption efficiency in cloud drops with higher numbers of soot cores



(Jacobson, 2006) and smaller E_{abs} in simulated ambient particles with larger number density of soot cores (Fierce et al., 2016). In addition, similar radiative absorption changes for soot-containing particles with different numbers of soot cores were observed during the transformation of soot core positions following the disappearance of liquid-liquid phase separation between organic and inorganic components (Zhang et al., 2022).

Based on the percentage, D_p/D_c , and E_{abs} of soot-containing particles with different mixing states and core numbers, we can compare the change in radiative absorption capacity per unit the change in coating thicknesses of soot-containing particles during the transboundary transport through the inland and the sea pathways. Figure 10b shows $\Delta E_{\text{abs}}/\Delta(D_p/D_c)$ of transboundary soot-containing particles transported through the inland and sea pathways. When soot-containing particles were transported from the NCP to the YRD through the inland pathway, their $\Delta E_{\text{abs}}/\Delta(D_p/D_c)$ reached 0.6 (Figure 10b). However, the $\Delta E_{\text{abs}}/\Delta(D_p/D_c)$ of soot-containing particles was only 0.17 following their transboundary transport through the sea pathway (Figure 10b). These findings suggest that the radiative absorption amplification per unit D_p/D_c change of transboundary soot-containing particles reduced by 72% with the change in their transport pathways from inland to sea. This can be ascribed to cloud processing during the transboundary transport through the sea pathway inducing more soot cores within single particles in contrast to the inland pathway, thereby reducing their optical absorption, as shown in Figure 11. Beeler et al. (2024) also found consistent results that much lower E_{abs} variation for soot-containing particles with the thickening of coatings in pyrocumulonimbus clouds compared to urban air. If embedded types in soot-containing particles were presumed as the traditional core-shell model, the $\Delta E_{\text{abs}}/\Delta(D_p/D_c)$ of transboundary soot-containing particles was extremely low at 0.01-0.03 (Table S2). This result shows a large difference from the optical absorption simulated with real mixing structures of soot-containing particles. Therefore, the atmospheric humidity condition during the transport of soot particles not only affects their aging processes but also influences their radiative absorption (Figure 11). In view



523 of that soot particles can be exposed to high-humidity atmospheric environments during
524 transboundary transport, climate models should incorporate multicore soot-containing
525 particles to refine current simulations of climate effects.

526

527 **4. Conclusions and implications**

528 Cold fronts triggered by the East Asian winter monsoon have frequently
529 transported substantial air pollutant loads from the NCP to downwind areas over 1000
530 kilometers away in recent years, significantly impacting the YRD region (Huang et al.,
531 2020; Zhao et al., 2021). To explore the variation in microphysical properties, mixing
532 states, and light absorption of soot particles in these haze pollutants and their aging
533 mechanisms during the transboundary transport, we conducted synchronized field
534 campaigns in December 2017 and December 2020 across the NCP and the YRD. Two
535 types of transboundary transport models (i.e., passing through the inland and the sea)
536 were identified based on transport pathways of haze plumes. According to the mixing
537 state of soot particles examined by TEM observations, they were divided into bare-like,
538 partly-coated, and embedded types. Meanwhile, the number of soot cores within
539 individual soot-containing particles was quantified.

540 Following the transboundary transport of haze pollutants through the inland
541 pathway, soot-containing particles underwent heterogeneous aging processes. This
542 aging process changed the dominated mixing state of soot-containing particles from
543 partly-coated types at 67% to embedded types at 71%, but the soot core number per
544 particle mainly remained at one. The median size and mean D_p/D_c of partly-coated and
545 embedded soot-containing particles increased from 396-464 nm and 2.37-2.85 to 435-
546 505 nm and 2.79-3.41 during the transboundary transport through the inland pathway
547 because of secondary aerosol formation on soot particles via heterogeneous reactions.
548 In addition, the soot core D_f increased from 1.81-1.90 to 1.84-1.93 under the
549 compacting effect of secondary coatings on soot aggregates. When soot-containing
550 particles were transported through the sea pathway, cloud process aging under
551 extremely high RH became their major evolution mechanisms. The cloud process aging



not only transformed the dominated soot-containing particles from partly-coated types at 62% to embedded types at 72% but also increased their soot core numbers from 1 to ≥ 3 . Compared to the inland pathway, the median size and mean D_p/D_c of partly-coated soot-containing particles and their soot core D_f showed similar variations during the transboundary transport through the sea pathway. However, these parameters for embedded soot-containing particles transported through the sea pathway represented larger increases from 446 nm, 2.92, and 1.89 in the NCP to 925 nm, 4.38, and 2.07 in the YRD.

Based on the optical simulation, transboundary soot-containing particles transported through the inland pathway exhibited a $\Delta E_{\text{abs}}/\Delta(D_p/D_c)$ of 0.6. Nevertheless, with the change in the transport pathway of soot-containing particles from the inland to the sea, the $\Delta E_{\text{abs}}/\Delta(D_p/D_c)$ reduced by 72% due to the entrainment of multiple soot cores by cloud processes. Our study demonstrates that soot particles, i.e., black carbon, undergo distinct evolutionary processes and exhibit altered microphysical and optical properties across different transport pathways. This necessitates incorporating meteorological conditions along transport pathways, particularly the elevated RH in sea pathways, into future assessments of black carbon optical properties. Given the scarce observational data on transboundary black carbon in the marine atmosphere compared to well-characterized those in the inland atmosphere, directly applying inland-based parameterization schemes to simulate optical properties of black carbon transported through sea pathways would introduce significant biases. Therefore, to accurately obtain optical properties of atmospheric transported black carbon, we suggest that future studies should prioritize multiscale characterization of black carbon mixing states and morphology in different transportation environments, particularly the cloud-processed mixing structure of multiple black carbon cores. Advanced single particle modeling, such as EMBS, that can reconstruct particles with real microphysical properties from TEM images could be coupled into macroscopic radiative forcing estimation (Wang et al., 2025). Ultimately, quantifying the climate impacts of black carbon necessitates a comprehensive understanding of how mixing state and



581 morphology evolution driven by atmospheric aging processes regulates absorption
582 enhancement to refine predictive models for climate mitigation strategies.



583 **Data availability**

584 All data presented in this paper are available upon request from the corresponding
585 author (liweijun@zju.edu.cn).

586

587 **Author contributions**

588 JZ and WL conceived the study and wrote the manuscript. The field campaigns
589 were organized and supervised by JZ and WL, and assisted by YW, LX, YZ, and HN.
590 JZ, YW, LX, and YZ contributed the sample analyses. ZZ made the optical simulation.
591 All authors reviewed and commented on the paper.

592

593 **Competing interests**

594 The authors declare that they have no conflict of interest.

595

596 **Acknowledgements**

597 This work was funded by the National Natural Science Foundation of China
598 (42307141 and 42307143), Shandong Provincial Natural Science Foundation of China
599 (ZR2023QD094 and ZR2023QD151), Zhejiang Provincial Natural Science Foundation
600 of China (LZJMZ25D050002), and LAC/CMA (2023B10). We thanked Wenshuai Li
601 for the sea level pressure simulation.



References

- Adachi, K., Zaizen, Y., Kajino, M., and Igarashi, Y.: Mixing state of regionally transported soot particles and the coating effect on their size and shape at a mountain site in Japan, *J. Geophys. Res.-Atmos.*, 119, 5386–5396, <https://doi.org/10.1002/2013jd020880>, 2014.
- Barone, T. L., Storey, J. M. E., Youngquist, A. D., and Szybist, J. P.: An analysis of direct-injection spark-ignition (DISI) soot morphology, *Atmos. Environ.*, 49, 268–274, <https://doi.org/10.1016/j.atmosenv.2011.11.047>, 2012.
- Beeler, P., Kumar, J., Schwarz, J. P., Adachi, K., Fierce, L., Perring, A. E., Katich, J. M., and Chakrabarty, R. K.: Light absorption enhancement of black carbon in a pyrocumulonimbus cloud, *Nat. Commun.*, 15, 6243, <https://doi.org/10.1038/s41467-024-50070-0>, 2024.
- Bond, T. C., and Bergstrom, R. W.: Light Absorption by Carbonaceous Particles: An Investigative Review, *Aerosol Sci. Tech.*, 40, 27–67, <https://doi.org/10.1080/02786820500421521>, 2006.
- Bond, T. C., Doherty, S. J., Fahey, D. W., Forster, P. M., Bernsten, T., DeAngelo, B. J., Flanner, M. G., Ghan, S., Kärcher, B., Koch, D., Kinne, S., Kondo, Y., Quinn, P. K., Sarofim, M. C., Schultz, M. G., Schulz, M., Venkataraman, C., Zhang, H., Zhang, S., Bellouin, N., Guttikunda, S. K., Hopke, P. K., Jacobson, M. Z., Kaiser, J. W., Klimont, Z., Lohmann, U., Schwarz, J. P., Shindell, D., Storelvmo, T., Warren, S. G., and Zender, C. S.: Bounding the role of black carbon in the climate system: A scientific assessment, *J. Geophys. Res.-Atmos.*, 118, 5380–5552, <https://doi.org/10.1002/jgrd.50171>, 2013.
- Cappa, C. D., Onasch, T. B., Massoli, P., Worsnop, D. R., Bates, T. S., Cross, E. S., Davidovits, P., Hakala, J., Hayden, K. L., Jobson, B. T., Kolesar, K. R., Lack, D. A., Lerner, B. M., Li, S. M., Mellon, D., Nuaaman, I., Olfert, J. S., Petaja, T., Quinn, P. K., Song, C., Subramanian, R., Williams, E. J., and Zaveri, R. A.: Radiative Absorption Enhancements Due to the Mixing State of Atmospheric Black Carbon, *Science*, 337, 1078–1081, <https://doi.org/10.1126/science.1223447>, 2012.
- Chen, X., Ye, C., Wang, Y., Wu, Z., Zhu, T., Zhang, F., Ding, X., Shi, Z., Zheng, Z., and Li, W.: Quantifying evolution of soot mixing state from transboundary transport of biomass burning emissions, *iScience*, 26, 108125, <https://doi.org/10.1016/j.isci.2023.108125>, 2023.
- China, S., Scarnato, B., Owen, R. C., Zhang, B., Ampadu, M. T., Kumar, S., Dzepina, K., Dziobak, M. P., Fialho, P., Perlanger, J. A., Hueber, J., Helmig, D., Mazzoleni, L. R., and Mazzoleni, C.: Morphology and mixing state of aged soot particles at a remote marine free troposphere site: Implications for optical properties, *Geophys. Res. Lett.*, 42, 1243–1250, <https://doi.org/10.1002/2014gl062404>, 2015.
- Ding, S., Liu, D., Zhao, S., Wu, Y., Li, S., Pan, B., Teng, X., Li, W., Xu, W., Zhang, Y., Sun, Y., Wu, Y., Pan, X., Peng, X., Zhang, G., Bi, X., Tian, P., Liu, L., and Wang, Z.: Field Observation of Important Nonactivation Scavenging of Black Carbon by Clouds, *Environ. Sci. Technol.*, 59, 9689–9698, <https://doi.org/10.1021/acs.est.5c00199>, 2025.
- Farley, R. N., Collier, S., Cappa, C. D., Williams, L. R., Onasch, T. B., Russell, L. M., Kim, H., and Zhang, Q.: Source apportionment of soot particles and aqueous-phase processing of black carbon coatings in an urban environment, *Atmos. Chem. Phys.*, 23, 15039–15056, <https://doi.org/10.5194/acp-23-15039-2023>, 2023.
- Fierce, L., Bond, T. C., Bauer, S. E., Mena, F., and Riemer, N.: Black carbon absorption at the global scale is affected by particle-scale diversity in composition, *Nat. Commun.*, 7, 12361, <https://doi.org/10.1038/ncomms12361>, 2016.



- 645 Fierce, L., Onasch, T. B., Cappa, C. D., Mazzoleni, C., China, S., Bhandari, J., Davidovits, P., Fischer,
646 D. A., Helgestad, T., Lambe, A. T., Sedlacek, A. J., Smith, G. D., and Wolff, L.: Radiative absorption
647 enhancements by black carbon controlled by particle-to-particle heterogeneity in composition,
648 *Proc. Natl. Acad. Sci. U. S. A.*, 117, 5196–5203, <https://doi.org/10.1073/pnas.1919723117>, 2020.
- 649 Fu, Y., Peng, X., Sun, W., Hu, X., Wang, D., Yang, Y., Guo, Z., Wang, Y., Zhang, G., Zhu, J., Ou, J., Shi,
650 Z., Wang, X., and Bi, X.: Impact of Cloud Process in the Mixing State and Microphysical Properties
651 of Soot Particles: Implications in Light Absorption Enhancement, *J. Geophys. Res.-Atmos.*, 127,
652 e2022JD037169, <https://doi.org/10.1029/2022JD037169>, 2022.
- 653 Geng, G., Zheng, Y., Zhang, Q., Xue, T., Zhao, H., Tong, D., Zheng, B., Li, M., Liu, F., Hong, C., He,
654 K., and Davis, S. J.: Drivers of PM_{2.5} air pollution deaths in China 2002–2017, *Nat. Geosci.*, 14, 645–
655 650, <https://doi.org/10.1038/s41561-021-00792-3>, 2021.
- 656 Han, C., Liu, Y., and He, H.: Role of Organic Carbon in Heterogeneous Reaction of NO₂ with Soot,
657 *Environ. Sci. Technol.*, 47, 3174–3181, <https://doi.org/10.1021/es304468n>, 2013.
- 658 Hou, X., Zhu, B., Kumar, K. R., de Leeuw, G., Lu, W., Huang, Q., and Zhu, X.: Establishment of
659 Conceptual Schemas of Surface Synoptic Meteorological Situations Affecting Fine Particulate
660 Pollution Across Eastern China in the Winter, *J. Geophys. Res.-Atmos.*, 125, e2020JD033153,
661 <https://doi.org/10.1029/2020JD033153>, 2020.
- 662 Huang, X., Ding, A., Wang, Z., Ding, K., Gao, J., Chai, F., and Fu, C.: Amplified transboundary
663 transport of haze by aerosol–boundary layer interaction in China, *Nat. Geosci.*, 13, 428–434,
664 <https://doi.org/10.1038/s41561-020-0583-4>, 2020.
- 665 IPCC: Climate Change 2021: the Physical Science Basis: Contribution of Working Group I to the
666 Sixth Assessment Report of the Intergovernmental Panel on Climate Change (IPCC). 2021.
- 667 Jacobson, M. Z.: Strong radiative heating due to the mixing state of black carbon in atmospheric
668 aerosols, *Nature*, 409, 695–697, <https://doi.org/10.1038/35055518>, 2001.
- 669 Jacobson, M. Z.: Effects of Externally-Through-Internally-Mixed Soot Inclusions within Clouds and
670 Precipitation on Global Climate, *J. Phys. Chem. A*, 110, 6860–6873,
671 <https://doi.org/10.1021/jp056391r>, 2006.
- 672 Jin, X., Cai, X., Huang, Q., Wang, X., Song, Y., and Zhu, T.: Atmospheric Boundary Layer—Free
673 Troposphere Air Exchange in the North China Plain and its Impact on PM_{2.5} Pollution, *J. Geophys.*
674 *Res.-Atmos.*, 126, e2021JD034641, <https://doi.org/10.1029/2021JD034641>, 2021.
- 675 Kang, H., Zhu, B., Gao, J., He, Y., Wang, H., Su, J., Pan, C., Zhu, T., and Yu, B.: Potential impacts of
676 cold frontal passage on air quality over the Yangtze River Delta, China, *Atmos. Chem. Phys.*, 19,
677 3673–3685, <https://doi.org/10.5194/acp-19-3673-2019>, 2019.
- 678 Li, B., Gasser, T., Ciais, P., Piao, S., Tao, S., Balkanski, Y., Hauglustaine, D., Boisier, J.-P., Chen, Z.,
679 Huang, M., Li, L. Z., Li, Y., Liu, H., Liu, J., Peng, S., Shen, Z., Sun, Z., Wang, R., Wang, T., Yin, G., Yin,
680 Y., Zeng, H., Zeng, Z., and Zhou, F.: The contribution of China's emissions to global climate forcing,
681 *Nature*, 531, 357–361, <https://doi.org/10.1038/nature17165>, 2016a.
- 682 Li, M., Wang, T., Xie, M., Li, S., Zhuang, B., Huang, X., Chen, P., Zhao, M., and Liu, J.: Formation and
683 Evolution Mechanisms for Two Extreme Haze Episodes in the Yangtze River Delta Region of China
684 During Winter 2016, *J. Geophys. Res.-Atmos.*, 124, 3607–3623,
685 <https://doi.org/10.1029/2019JD030535>, 2019.
- 686 Li, W., Sun, J., Xu, L., Shi, Z., Riemer, N., Sun, Y., Fu, P., Zhang, J., Lin, Y., Wang, X., Shao, L., Chen, J.,
687 Zhang, X., Wang, Z., and Wang, W.: A conceptual framework for mixing structures in individual
688 aerosol particles, *J. Geophys. Res.-Atmos.*, 121, 13784–13798,



- 689 <https://doi.org/10.1002/2016JD025252>, 2016b.
- 690 Li, W., Riemer, N., Xu, L., Wang, Y., Adachi, K., Shi, Z., Zhang, D., Zheng, Z., and Laskin, A.:
691 Microphysical properties of atmospheric soot and organic particles: measurements, modeling, and
692 impacts, *npj Clim. Atmos. Sci.*, 7, 65, <https://doi.org/10.1038/s41612-024-00610-8>, 2024.
- 693 Li, W., Ito, A., Wang, G., Zhi, M., Xu, L., Yuan, Q., Zhang, J., Liu, L., Wu, F., Laskin, A., Zhang, D.,
694 Zhang, X., Zhu, T., Chen, J., Mihalopoulos, N., Bougiatioti, A., Kanakidou, M., Wang, G., Hu, H., Zhao,
695 Y., and Shi, Z.: Aqueous-phase secondary organic aerosol formation on mineral dust, *Natl. Sci.*
696 *Rev.*, 12, nwaf221, <https://doi.org/10.1093/nsr/nwaf221>, 2025.
- 697 Liu, D., He, C., Schwarz, J. P., and Wang, X.: Lifecycle of light-absorbing carbonaceous aerosols in
698 the atmosphere, *npj Clim. Atmos. Sci.*, 3, 40, <https://doi.org/10.1038/s41612-020-00145-8>, 2020.
- 699 Liu, L., Zhang, J., Xu, L., Yuan, Q., Huang, D., Chen, J., Shi, Z., Sun, Y., Fu, P., Wang, Z., Zhang, D.,
700 and Li, W.: Cloud scavenging of anthropogenic refractory particles at a mountain site in North
701 China, *Atmos. Chem. Phys.*, 18, 14681–14693, <https://doi.org/10.5194/acp-18-14681-2018>, 2018.
- 702 Niu, H., Hu, W., Zhang, D., Wu, Z., Guo, S., Pian, W., Cheng, W., and Hu, M.: Variations of fine
703 particle physiochemical properties during a heavy haze episode in the winter of Beijing, *Sci. Total*
704 *Environ.*, 571, 103–109, <https://doi.org/10.1016/j.scitotenv.2016.07.147>, 2016.
- 705 Oh, C., and Sorensen, C. M.: The Effect of Overlap between Monomers on the Determination of
706 Fractal Cluster Morphology, *J. Colloid Interface Sci.*, 193, 17–25,
707 <https://doi.org/10.1006/jcis.1997.5046>, 1997.
- 708 Pan, Y., Wang, Y., Sun, Y., Tian, S., and Cheng, M.: Size-resolved aerosol trace elements at a rural
709 mountainous site in Northern China: importance of regional transport, *Sci. Total Environ.*, 461–462,
710 761–771, <https://doi.org/10.1016/j.scitotenv.2013.04.065>, 2013.
- 711 Pang, Y., Wang, Y., Wang, Z., Zhang, Y., Liu, L., Kong, S., Liu, F., Shi, Z., and Li, W.: Quantifying the
712 Fractal Dimension and Morphology of Individual Atmospheric Soot Aggregates, *J. Geophys. Res.-*
713 *Atmos.*, 127, e2021JD036055, <https://doi.org/10.1029/2021JD036055>, 2022.
- 714 Peng, J., Hu, M., Shang, D., Wu, Z., Du, Z., Tan, T., Wang, Y., Zhang, F., and Zhang, R.: Explosive
715 Secondary Aerosol Formation during Severe Haze in the North China Plain, *Environ. Sci. Technol.*,
716 55, 2189–2207, <https://doi.org/10.1021/acs.est.0c07204>, 2021.
- 717 Schnitzler, E. G., Gac, J. M., and Jäger, W.: Coating surface tension dependence of soot aggregate
718 restructuring, *J. Aerosol Sci.*, 106, 43–55, <https://doi.org/10.1016/j.jaerosci.2017.01.005>, 2017.
- 719 Suzuki, K., and Takemura, T.: Perturbations to Global Energy Budget Due to Absorbing and
720 Scattering Aerosols, *J. Geophys. Res.-Atmos.*, 124, 2194–2209,
721 <https://doi.org/10.1029/2018jd029808>, 2019.
- 722 Wang, J., Liu, D., Ge, X., Wu, Y., Shen, F., Chen, M., Zhao, J., Xie, C., Wang, Q., Xu, W., Zhang, J., Hu,
723 J., Allan, J., Joshi, R., Fu, P., Coe, H., and Sun, Y.: Characterization of black carbon-containing fine
724 particles in Beijing during wintertime, *Atmos. Chem. Phys.*, 19, 447–458,
725 <https://doi.org/10.5194/acp-19-447-2019>, 2019.
- 726 Wang, Q., Huang, R.-J., Zhao, Z., Cao, J., Ni, H., Tie, X., Zhao, S., Su, X., Han, Y., Shen, Z., Wang, Y.,
727 Zhang, N., Zhou, Y., and Corbin, J. C.: Physicochemical characteristics of black carbon aerosol and
728 its radiative impact in a polluted urban area of China, *J. Geophys. Res.-Atmos.*, 121, 12505–12519,
729 <https://doi.org/10.1002/2016JD024748>, 2016.
- 730 Wang, Y., Pang, Y., Huang, J., Bi, L., Che, H., Zhang, X., and Li, W.: Constructing Shapes and Mixing
731 Structures of Black Carbon Particles With Applications to Optical Calculations, *J. Geophys. Res.-*
732 *Atmos.*, 126, e2021JD034620, <https://doi.org/10.1029/2021JD034620>, 2021.



- 733 Wang, Y., Zheng, Z., Sun, Y., Yao, Y., Ma, P.-L., Zhang, A., Zhu, S., Zhang, Z., Chen, X., Pang, Y.,
734 Wang, Q., Che, H., Ching, J., and Li, W.: Improved representation of black carbon mixing structures
735 suggests stronger direct radiative heating, *One Earth*, 8,
736 <https://doi.org/10.1016/j.oneear.2025.101311>, 2025.
- 737 Worringer, A., Ebert, M., Trautmann, T., Weinbruch, S., and Helas, G.: Optical properties of
738 internally mixed ammonium sulfate and soot particles- a study of individual aerosol particles and
739 ambient aerosol populations, *Appl. Opt.*, 47, 3835-3845, <https://doi.org/10.1364/AO.47.003835>,
740 2008.
- 741 Wu, J., Bei, N., Li, X., Wang, R., Liu, S., Jiang, Q., Tie, X., and Li, G.: Impacts of Transboundary
742 Transport on Coastal Air Quality of South China, *J. Geophys. Res.-Atmos.*, 127, e2021JD036213,
743 <https://doi.org/10.1029/2021JD036213>, 2022.
- 744 Wu, Y., Cheng, T., Zheng, L., and Chen, H.: Optical properties of the semi-external mixture
745 composed of sulfate particle and different quantities of soot aggregates, *J. Quant. Spectrosc.*
746 *Radiat. Transfer*, 179, 139-148, <https://doi.org/10.1016/j.jqsrt.2016.03.012>, 2016.
- 747 Wu, Y., Cheng, T., Liu, D., Allan, J. D., Zheng, L., and Chen, H.: Light Absorption Enhancement of
748 Black Carbon Aerosol Constrained by Particle Morphology, *Environ. Sci. Technol.*, 52, 6912-6919,
749 <https://doi.org/10.1021/acs.est.8b00636>, 2018.
- 750 Xie, X., Hu, J., Qin, M., Guo, S., Hu, M., Ji, D., Wang, H., Lou, S., Huang, C., Liu, C., Zhang, H., Ying,
751 Q., Liao, H., and Zhang, Y.: Evolution of atmospheric age of particles and its implications for the
752 formation of a severe haze event in eastern China, *Atmos. Chem. Phys.*, 23, 10563-10578,
753 <https://doi.org/10.5194/acp-23-10563-2023>, 2023.
- 754 Xing, L., Fu, T. M., Cao, J. J., Lee, S. C., Wang, G. H., Ho, K. F., Cheng, M. C., You, C. F., and Wang, T.
755 J.: Seasonal and spatial variability of the OM/OC mass ratios and high regional correlation between
756 oxalic acid and zinc in Chinese urban organic aerosols, *Atmos. Chem. Phys.*, 13, 4307-4318,
757 <https://doi.org/10.5194/acp-13-4307-2013>, 2013.
- 758 Xu, L., Fukushima, S., Sobanska, S., Murata, K., Naganuma, A., Liu, L., Wang, Y., Niu, H., Shi, Z.,
759 Kojima, T., Zhang, D., and Li, W.: Tracing the evolution of morphology and mixing state of soot
760 particles along with the movement of an Asian dust storm, *Atmos. Chem. Phys.*, 20, 14321-14332,
761 <https://doi.org/10.5194/acp-20-14321-2020>, 2020.
- 762 Yan, F., Su, H., Cheng, Y., Huang, R., Liao, H., Yang, T., Zhu, Y., Zhang, S., Sheng, L., Kou, W., Zeng,
763 X., Xiang, S., Yao, X., Gao, H., and Gao, Y.: Frequent haze events associated with transport and
764 stagnation over the corridor between the North China Plain and Yangtze River Delta, *Atmos. Chem.*
765 *Phys.*, 24, 2365-2376, <https://doi.org/10.5194/acp-24-2365-2024>, 2024.
- 766 Yuan, Q., Xu, J., Wang, Y., Zhang, X., Pang, Y., Liu, L., Bi, L., Kang, S., and Li, W.: Mixing State and
767 Fractal Dimension of Soot Particles at a Remote Site in the Southeastern Tibetan Plateau, *Environ.*
768 *Sci. Technol.*, 53, 8227-8234, <https://doi.org/10.1021/acs.est.9b01917>, 2019.
- 769 Zang, H., Zhao, Y., Huo, J., Zhao, Q., Fu, Q., Duan, Y., Shao, J., Huang, C., An, J., Xue, L., Li, Z., Li, C.,
770 and Xiao, H.: High atmospheric oxidation capacity drives wintertime nitrate pollution in the eastern
771 Yangtze River Delta of China, *Atmos. Chem. Phys.*, 22, 4355-4374, <https://doi.org/10.5194/acp-22-4355-2022>, 2022.
- 772
- 773 Zhai, S., Jacob, D. J., Wang, X., Liu, Z., Wen, T., Shah, V., Li, K., Moch, J. M., Bates, K. H., Song, S.,
774 Shen, L., Zhang, Y., Luo, G., Yu, F., Sun, Y., Wang, L., Qi, M., Tao, J., Gui, K., Xu, H., Zhang, Q., Zhao,
775 T., Wang, Y., Lee, H. C., Choi, H., and Liao, H.: Control of particulate nitrate air pollution in China,
776 *Nat. Geosci.*, 14, 389-395, <https://doi.org/10.1038/s41561-021-00726-z>, 2021.



777 Zhang, J., Liu, L., Wang, Y., Ren, Y., Wang, X., Shi, Z., Zhang, D., Che, H., Zhao, H., Liu, Y., Niu, H.,
778 Chen, J., Zhang, X., Lingaswamy, A. P., Wang, Z., and Li, W.: Chemical composition, source, and
779 process of urban aerosols during winter haze formation in Northeast China, *Environ. Pollut.*, 231,
780 357–366, <https://doi.org/10.1016/j.envpol.2017.07.102>, 2017a.
781 Zhang, J., Yuan, Q., Liu, L., Wang, Y., Zhang, Y., Xu, L., Pang, Y., Zhu, Y., Niu, H., Shao, L., Yang, S.,
782 Liu, H., Pan, X., Shi, Z., Hu, M., Fu, P., and Li, W.: Trans-Regional Transport of Haze Particles From
783 the North China Plain to Yangtze River Delta During Winter, *J. Geophys. Res.-Atmos.*, 126,
784 e2020JD033778, <https://doi.org/10.1029/2020JD033778>, 2021.
785 Zhang, J., Wang, Y., Teng, X., Liu, L., Xu, Y., Ren, L., Shi, Z., Zhang, Y., Jiang, J., Liu, D., Hu, M., Shao,
786 L., Chen, J., Martin, S. T., Zhang, X., and Li, W.: Liquid-liquid phase separation reduces radiative
787 absorption by aged black carbon aerosols, *Commun. Earth Environ.*, 3, 128,
788 <https://doi.org/10.1038/s43247-022-00462-1>, 2022.
789 Zhang, J., Li, W., Wang, Y., Teng, X., Zhang, Y., Xu, L., Yuan, Q., Wu, G., Niu, H., and Shao, L.:
790 Structural Collapse and Coating Composition Changes of Soot Particles During Long-Range
791 Transport, *J. Geophys. Res.-Atmos.*, 128, e2023JD038871, <https://doi.org/10.1029/2023JD038871>,
792 2023.
793 Zhang, Q., Jiang, X., Tong, D., Davis, S. J., Zhao, H., Geng, G., Feng, T., Zheng, B., Lu, Z., and Streets,
794 D. G.: Transboundary health impacts of transported global air pollution and international trade,
795 *Nature*, 543, 705–709, <https://doi.org/10.1038/nature21712>, 2017b.
796 Zhang, W., Zhang, Y.-L., Cao, F., Xiang, Y., Zhang, Y., Bao, M., Liu, X., Lin, Y.-C. J. A. C., and Physics:
797 High time-resolved measurement of stable carbon isotope composition in water-soluble organic
798 aerosols: method optimization and a case study during winter haze in eastern China, *Atmos. Chem.*
799 *Phys.*, 19, 11071–11087, <https://doi.org/10.5194/acp-19-11071-2019>, 2019a.
800 Zhang, Y., Zhang, Q., Cheng, Y., Su, H., Li, H., Li, M., Zhang, X., Ding, A., and He, K.: Amplification
801 of light absorption of black carbon associated with air pollution, *Atmos. Chem. Phys.*, 18, 9879–
802 9896, <https://doi.org/10.5194/acp-18-9879-2018>, 2018.
803 Zhang, Y., Li, M., Cheng, Y., Geng, G., Hong, C., Li, H., Li, X., Tong, D., Wu, N., Zhang, X., Zheng, B.,
804 Zheng, Y., Bo, Y., Su, H., and Zhang, Q.: Modeling the aging process of black carbon during
805 atmospheric transport using a new approach: a case study in Beijing, *Atmos. Chem. Phys.*, 19,
806 9663–9680, <https://doi.org/10.5194/acp-19-9663-2019>, 2019b.
807 Zhao, J., Qiu, Y., Zhou, W., Xu, W., Wang, J., Zhang, Y., Li, L., Xie, C., Wang, Q., Du, W., Worsnop, D.
808 R., Canagaratna, M. R., Zhou, L., Ge, X., Fu, P., Li, J., Wang, Z., Donahue, N. M., and Sun, Y.: Organic
809 Aerosol Processing During Winter Severe Haze Episodes in Beijing, *J. Geophys. Res.-Atmos.*, 124,
810 10248–10263, <https://doi.org/10.1029/2019jd030832>, 2019.
811 Zhao, S., Feng, T., Tie, X., Li, G., and Cao, J.: Air Pollution Zone Migrates South Driven by East Asian
812 Winter Monsoon and Climate Change, *Geophys. Res. Lett.*, 48, e2021GL092672,
813 <https://doi.org/10.1029/2021GL092672>, 2021.
814 Zheng, G. J., Duan, F. K., Su, H., Ma, Y. L., Cheng, Y., Zheng, B., Zhang, Q., Huang, T., Kimoto, T.,
815 Chang, D., Pöschl, U., Cheng, Y. F., and He, K. B.: Exploring the severe winter haze in Beijing: the
816 impact of synoptic weather, regional transport and heterogeneous reactions, *Atmos. Chem. Phys.*,
817 15, 2969–2983, <https://doi.org/10.5194/acp-15-2969-2015>, 2015.
818 Zhong, J., Zhang, X., Wang, Y., Wang, J., Shen, X., Zhang, H., Wang, T., Xie, Z., Liu, C., Zhang, H.,
819 Zhao, T., Sun, J., Fan, S., Gao, Z., Li, Y., and Wang, L.: The two-way feedback mechanism between
820 unfavorable meteorological conditions and cumulative aerosol pollution in various haze regions



821 of China, Atmos. Chem. Phys., 19, 3287–3306, <https://doi.org/10.5194/acp-19-3287-2019>, 2019.
822 Zhu, J., Wu, S., Yue, H., Gao, E., Wang, W., Li, J., Wu, Z., and Yao, S.: Enhanced oxidative potential
823 and SO₂ heterogeneous oxidation on candle soot after photochemical aging: Influencing
824 mechanisms of different irradiation wavelengths, Environ. Pollut., 367, 125583,
825 <https://doi.org/10.1016/j.envpol.2024.125583>, 2025.

826



Figure Captions

827

828 **Figure 1.** Meteorological fields in eastern China during the observation period. (a-b)
829 Wind fields combined with surface PM_{2.5} concentrations at 20:00 (local time) on
830 December 30, 2017 and at 2:00 on December 8, 2020 derived from European Centre
831 for Medium-Range Weather Forecasts (ECMWF, <https://earth.nullschool.net/>). The
832 blue arrow dashed lines indicate prevailing wind direction. (c-d) Meteorological fields
833 covering observation sites in the North China Plain (NCP) and Yangtze River Delta
834 (YRD) at 1000 hpa.

835 **Figure 2.** Concentration-weighted trajectory (CWT) plots of PM_{2.5} before arriving at
836 observation sites in the YRD. (a-b) Nanjing and Hangzhou during December 30-31,
837 2017. (c-d) Nanjing and Hangzhou during December 7-8, 2020.

838 **Figure 3.** Typical transmission electron microscopy (TEM) images of soot particles in
839 different mixing states. (a) Bare-like soot particle. (b) Partly-coated soot particles. (c)
840 Embedded soot particles. Embedded soot particles in panel (c) can be clearly observed
841 after their coatings are sublimed under strong electron beam.

842 **Figure 4.** Typical TEM images and number fractions of soot-containing particles with
843 different mixing states and soot core numbers in two types of transboundary transport
844 models from the NCP to the YRD. (a) Partly-coated and embedded soot-containing
845 particles with different numbers of soot cores. (b) Variation in the number fraction of
846 soot-containing particles during the transboundary transport through the inland pathway.
847 (c) Variation in the number fraction of soot-containing particles during the
848 transboundary transport through the sea pathway.

849 **Figure 5.** Number fractions of soot-containing particles with different mixing states
850 and numbers of soot cores in different size bins in two types of transboundary transport
851 models from the NCP to the YRD. (a-b) Soot-containing particles transported through
852 the inland pathway. (c-d) Soot-containing particles transported through the sea pathway.

853 **Figure 6.** Number size distribution of soot-containing particles in two types of
854 transboundary transport models from the NCP to the YRD. (a-b) Size distribution of
855 soot-containing particles transported through the inland pathway. (c-d) Size distribution



856 of soot-containing particles transported through the sea pathway.

857 **Figure 7.** The size ratio of soot-containing particles to their soot cores (D_p/D_c) in two
858 types of transboundary transport models from the NCP to the YRD. (a) D_p/D_c ratios of
859 soot-containing particles transported through the inland pathway. (b) D_p/D_c ratios of
860 soot-containing particles transported through the sea pathway. A schematic model of
861 the D_p/D_c ratio of soot-containing particles with the core-shell structure is exemplified.

862 **Figure 8.** Low magnification TEM images of soot-containing particles in the YRD
863 during two transboundary transport. (a) Soot-containing particles transported through
864 the inland pathway. (b) Soot-containing particles transported through the sea pathway.
865 (c-d) Magnified TEM images for soot-containing particles in panel (a). (e-f) Magnified
866 TEM images for soot-containing particles in panel (b).

867 **Figure 9.** Variation in the fractal dimension (D_f) of partly-coated and embedded soot
868 particles during their transboundary transport from the NCP to the YRD. (a-b) D_f of
869 soot particles transported through the inland pathway. (c-d) D_f of soot particles
870 transported through the sea pathway. A schematic model of the soot D_f is exemplified.

871 **Figure 10.** Variation in the optical absorption of soot-containing particles. (a) The light
872 absorption enhancement (E_{abs}) of partly-coated and embedded soot-containing particle
873 models relative to their soot cores. (b) The change in E_{abs} per unit the change in D_p/D_c
874 ($\Delta E_{abs}/\Delta(D_p/D_c)$) of soot-containing particles during two transboundary transport
875 events through the inland and the sea pathways. Partly-coated and embedded soot-
876 containing particle models constructed by the Electron-Microscope-to-BC-Simulation
877 (EMBS) tool were exemplified in panel (a).

878 **Figure 11.** A schematic diagram for the change in the mixing state and optical
879 absorption of soot-containing particles during the transboundary transport from the
880 NCP to the YRD through the inland and the sea pathways. (a) Soot-containing particles
881 undergo heterogeneous aging processes during the transboundary transport through the
882 inland pathway, which mainly change their mixing states from partly-coated with single
883 soot core to embedded with single soot core structures and increase the E_{abs} change per
884 unit D_p/D_c change at 0.6. (b) Following the transboundary transport of soot-containing



885 particles through the sea pathway, cloud process aging becomes the dominated
886 evolution mechanism of soot-containing particles. This process not only transforms the
887 mixing state of soot-containing particles from partly-coated with single soot core to
888 embedded with multiple soot core structures but also slightly enhances the E_{abs} change
889 per unit D_p/D_c change at 0.17.

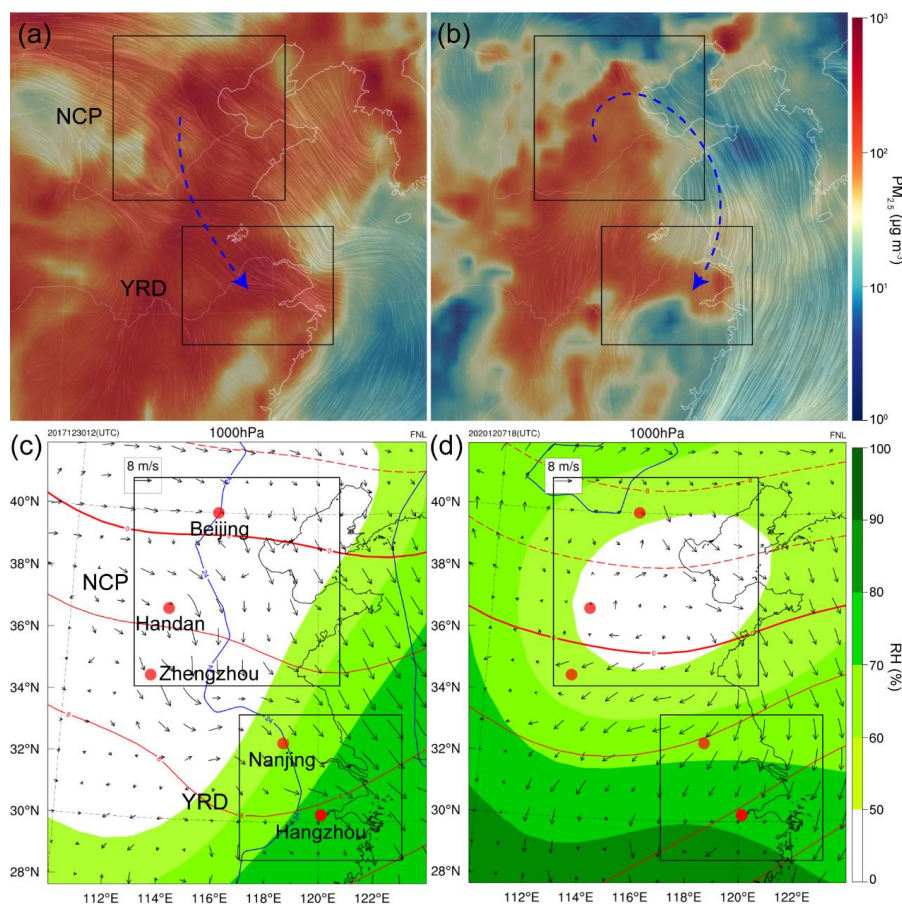


Figure 1. Meteorological fields in eastern China during the observation period. (a-b) Wind fields combined with surface $PM_{2.5}$ concentrations at 20:00 (local time) on December 30, 2017 and at 2:00 on December 8, 2020 derived from European Centre for Medium-Range Weather Forecasts (ECMWF, <https://earth.nullschool.net/>). The blue arrow dashed lines indicate prevailing wind direction. (c-d) Meteorological fields covering observation sites in the North China Plain (NCP) and Yangtze River Delta (YRD) at 1000 hpa.

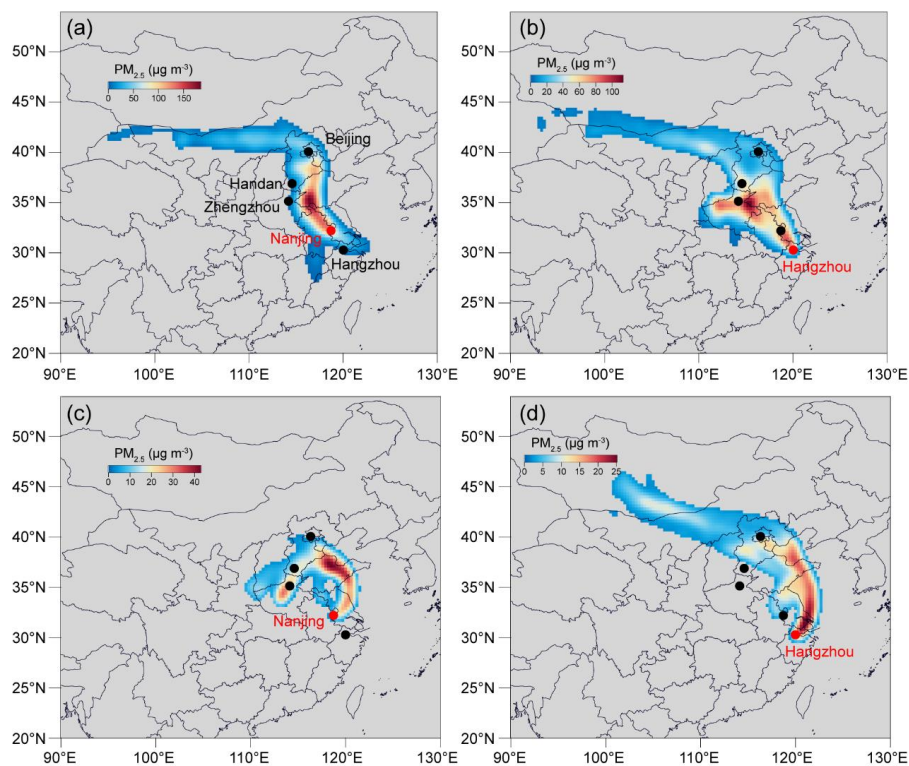


Figure 2. Concentration-weighted trajectory (CWT) plots of $PM_{2.5}$ before arriving at observation sites in the YRD. (a-b) Nanjing and Hangzhou during December 30-31, 2017. (c-d) Nanjing and Hangzhou during December 7-8, 2020.

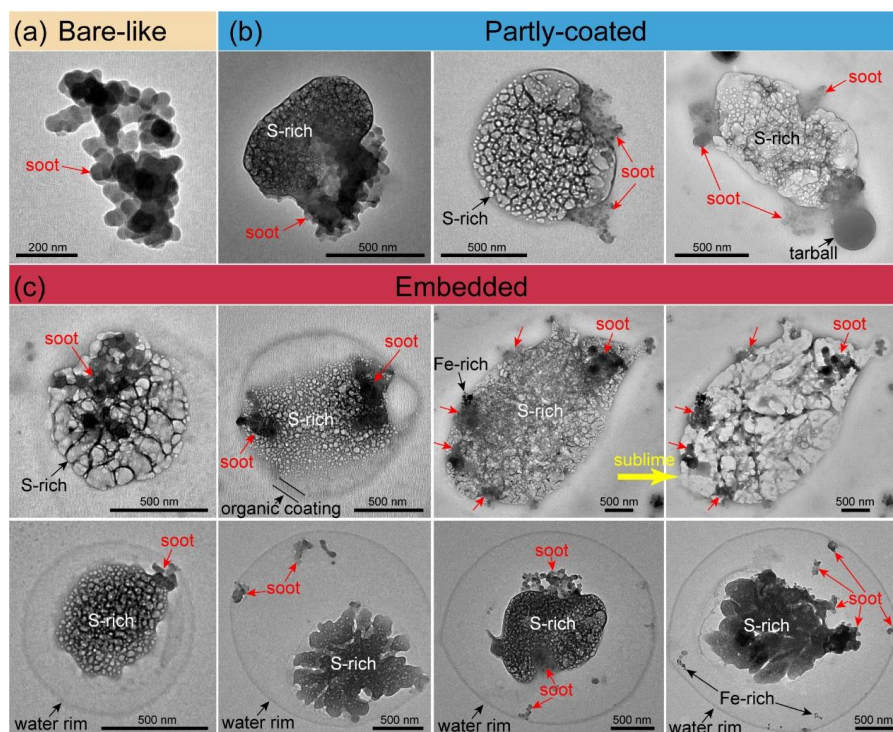


Figure 3. Typical transmission electron microscopy (TEM) images of soot particles in different mixing states. (a) Bare-like soot particle. (b) Partly-coated soot particles. (c) Embedded soot particles. Embedded soot particles in panel (c) can be clearly observed after their coatings are sublimed under strong electron beam.

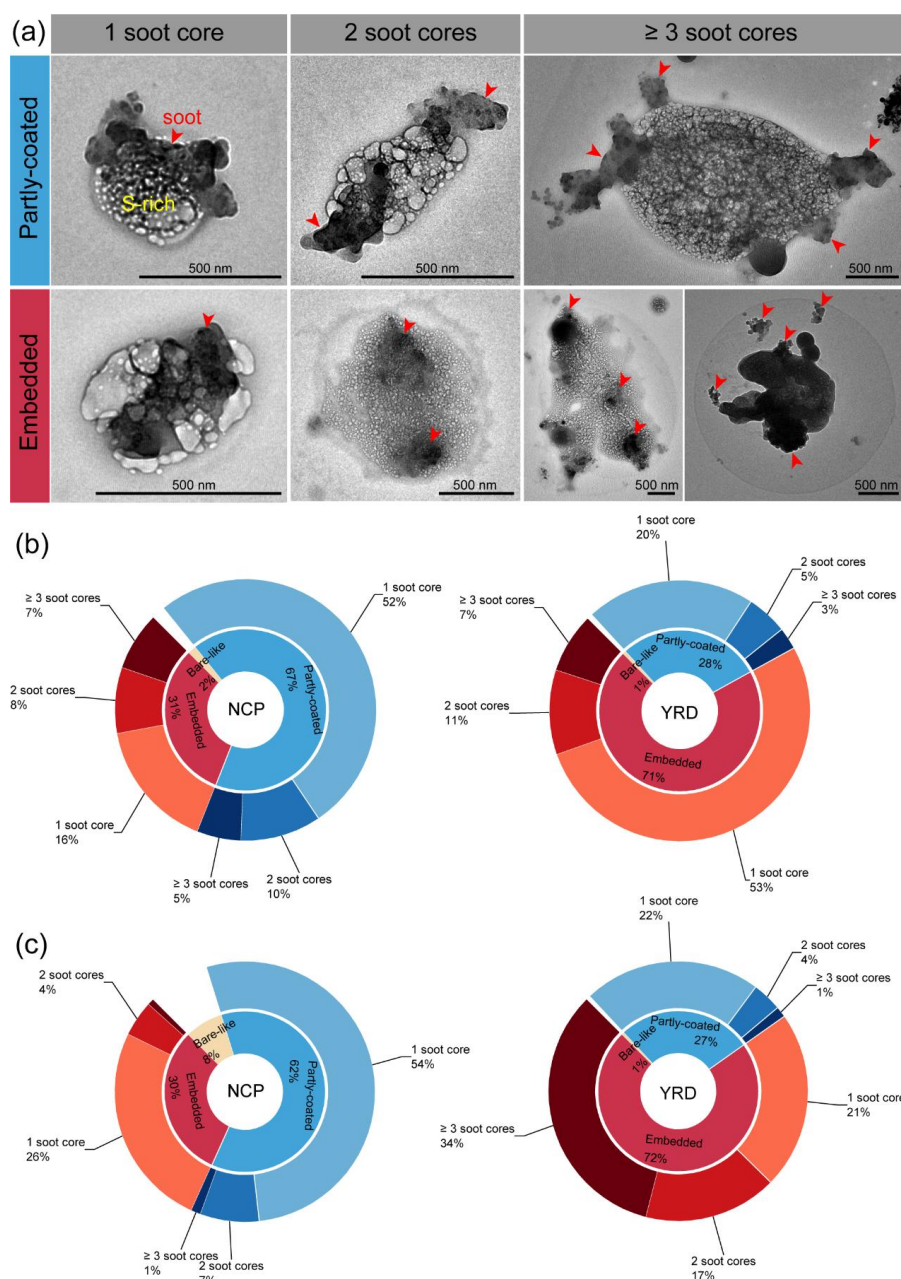
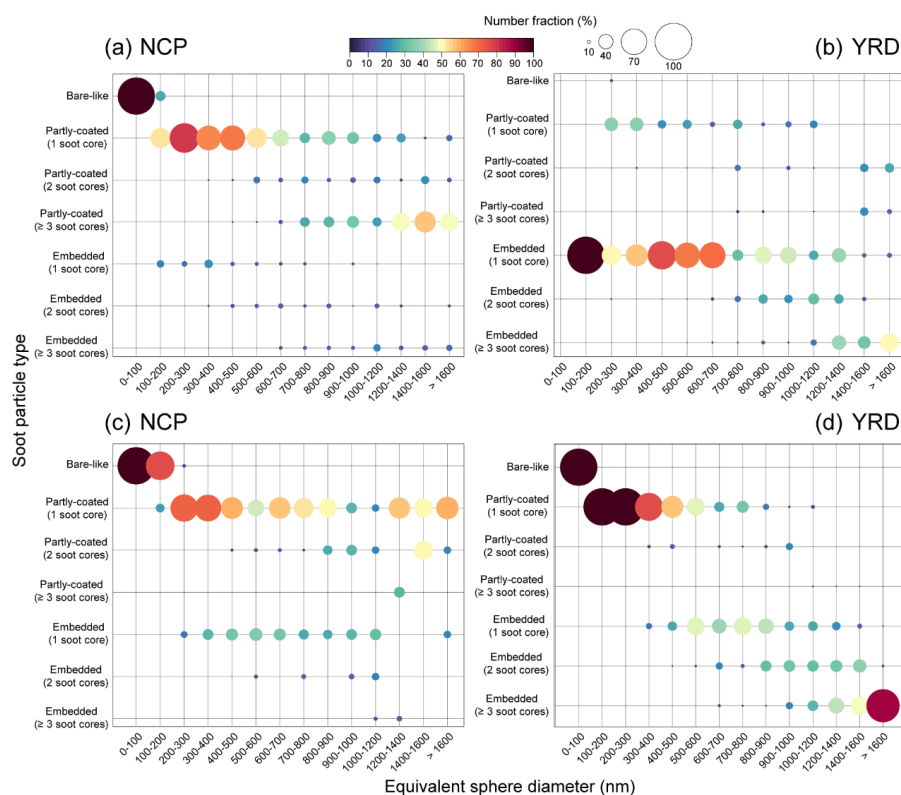


Figure 4. Typical TEM images and number fractions of soot-containing particles with different mixing states and soot core numbers in two types of transboundary transport models from the NCP to the YRD. (a) Partly-coated and embedded soot-containing particles with different numbers of soot cores. (b) Variation in the number fraction of

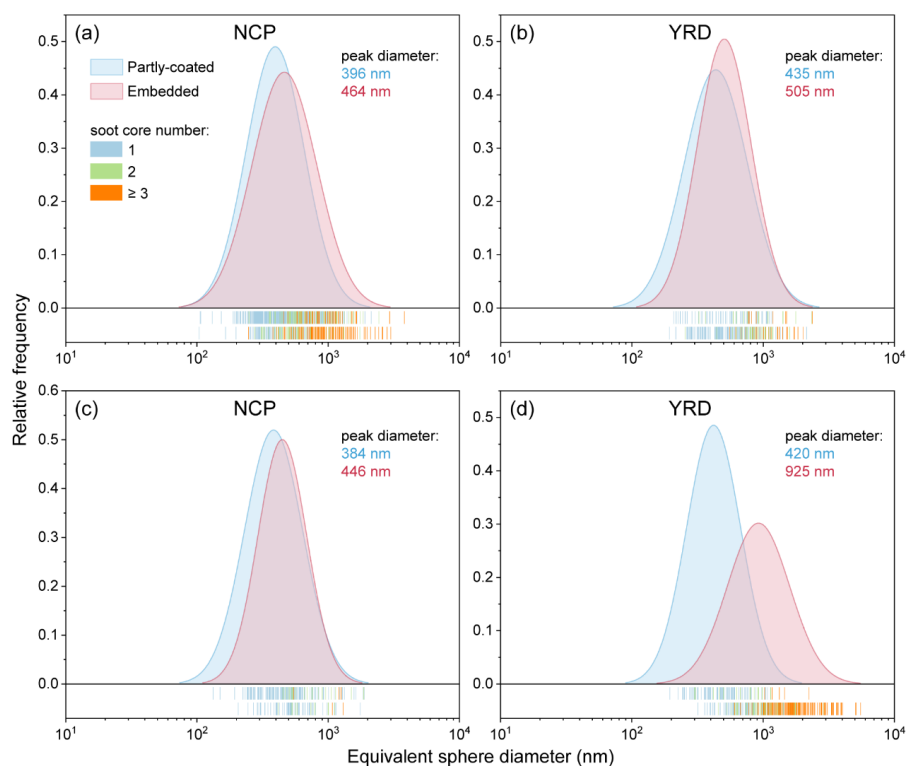


912 soot-containing particles during the transboundary transport through the inland pathway.
913 (c) Variation in the number fraction of soot-containing particles during the
914 transboundary transport through the sea pathway.



915

916 **Figure 5.** Number fractions of soot-containing particles with different mixing states
 917 and numbers of soot cores in different size bins in two types of transboundary transport
 918 models from the NCP to the YRD. (a-b) Soot-containing particles transported through
 919 the inland pathway. (c-d) Soot-containing particles transported through the sea pathway.



920

921 **Figure 6.** Number size distribution of soot-containing particles in two types of
922 transboundary transport models from the NCP to the YRD. (a-b) Size distribution of
923 soot-containing particles transported through the inland pathway. (c-d) Size distribution
924 of soot-containing particles transported through the sea pathway.

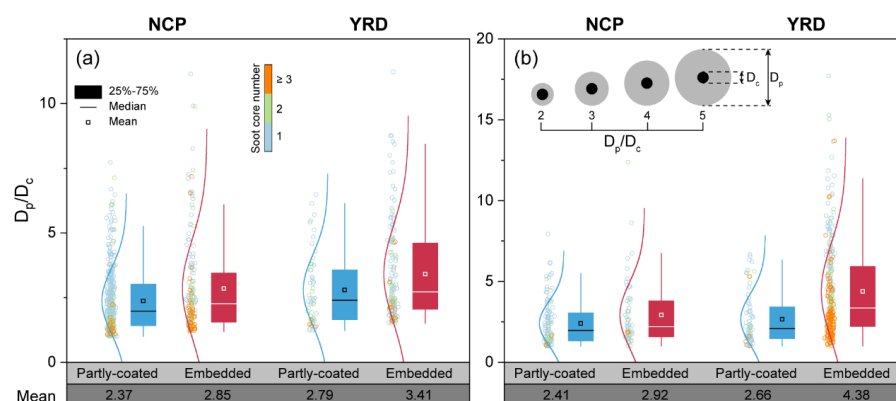


Figure 7. The size ratio of soot-containing particles to their soot cores (D_p/D_c) in two types of transboundary transport models from the NCP to the YRD. (a) D_p/D_c ratios of soot-containing particles transported through the inland pathway. (b) D_p/D_c ratios of soot-containing particles transported through the sea pathway. A schematic model of the D_p/D_c ratio of soot-containing particles with the core-shell structure is exemplified.

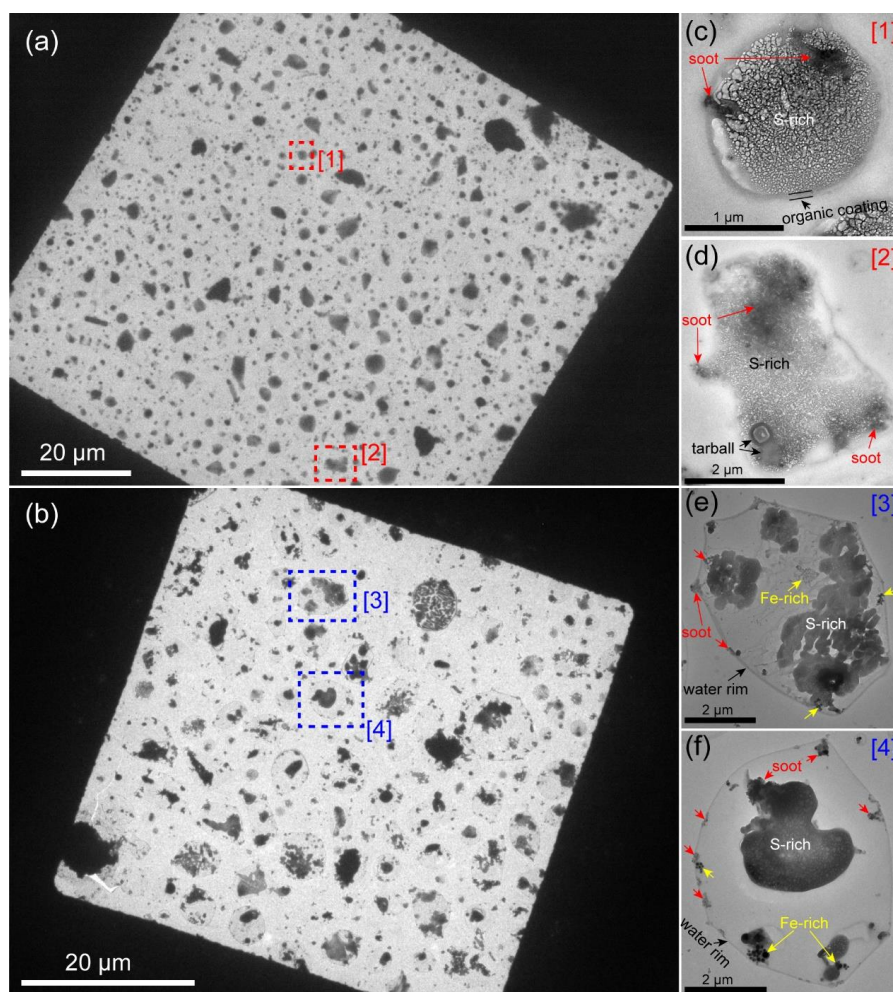
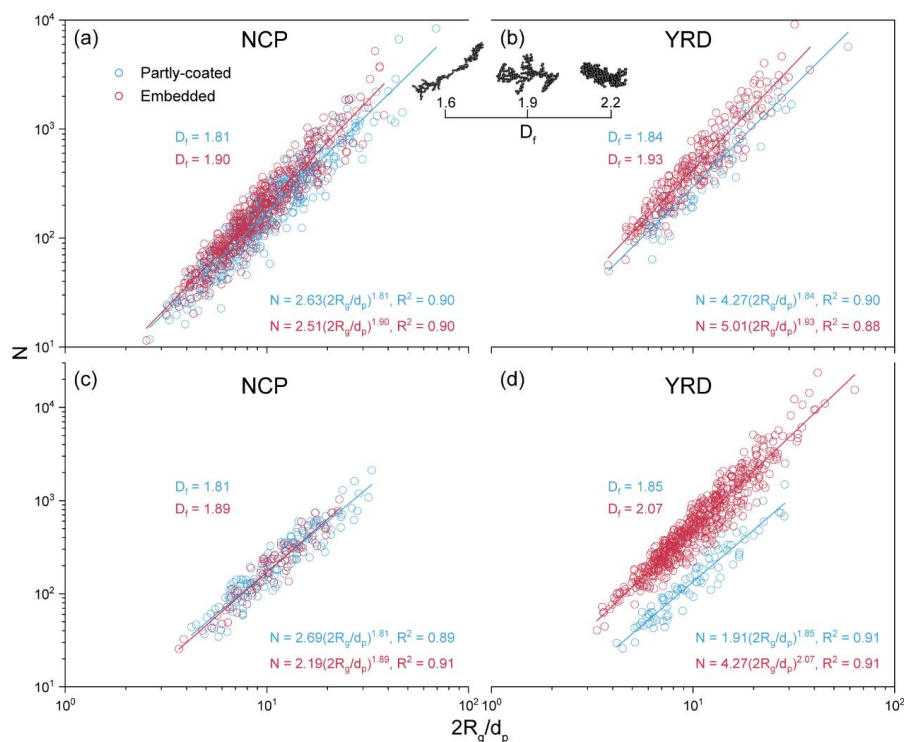
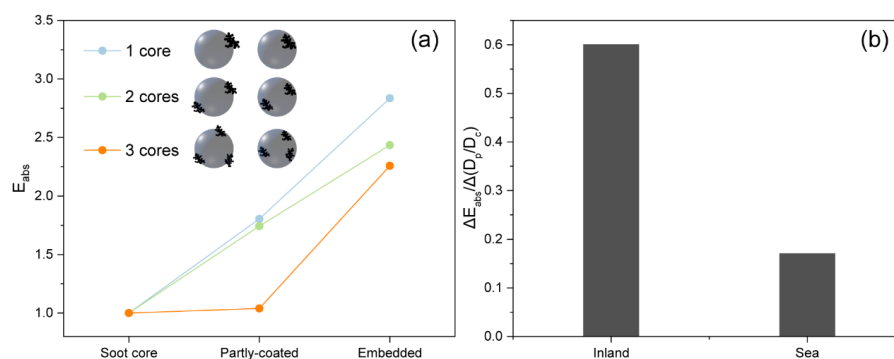


Figure 8. Low magnification TEM images of soot-containing particles in the YRD during two transboundary transport. (a) Soot-containing particles transported through the inland pathway. (b) Soot-containing particles transported through the sea pathway. (c-d) Magnified TEM images for soot-containing particles in panel (a). (e-f) Magnified TEM images for soot-containing particles in panel (b).



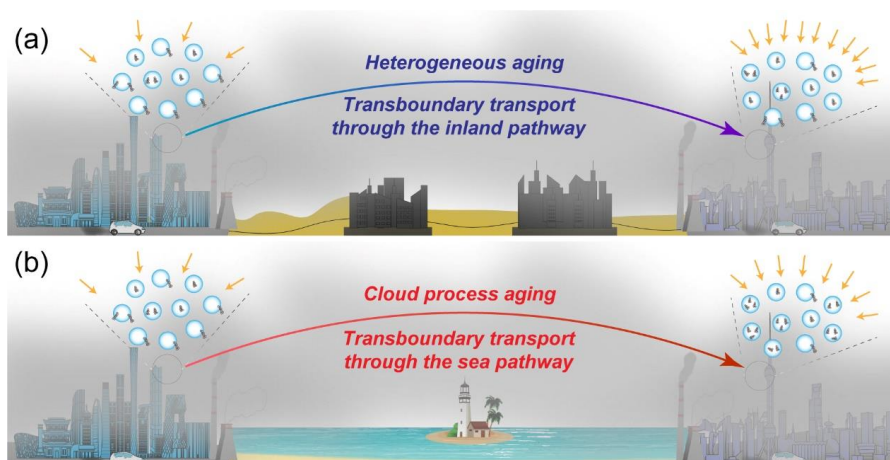
937

938 **Figure 9.** Variation in the fractal dimension (D_f) of partly-coated and embedded soot
 939 particles during their transboundary transport from the NCP to the YRD. (a-b) D_f of
 940 soot particles transported through the inland pathway. (c-d) D_f of soot particles
 941 transported through the sea pathway. A schematic model of the soot D_f is exemplified.



942

943 **Figure 10.** Variation in the optical absorption of soot-containing particles. (a) The light
944 absorption enhancement (E_{abs}) of partly-coated and embedded soot-containing particle
945 models relative to their soot cores. (b) The change in E_{abs} per unit the change in D_p/D_c
946 ($\Delta E_{abs}/\Delta(D_p/D_c)$) of soot-containing particles during two transboundary transport
947 events through the inland and the sea pathways. Partly-coated and embedded soot-
948 containing particle models constructed by the Electron-Microscope-to-BC-Simulation
949 (EMBS) tool were exemplified in panel (a).



950

951 **Figure 11.** A schematic diagram for the change in the mixing state and optical
 952 absorption of soot-containing particles during the transboundary transport from the
 953 NCP to the YRD through the inland and the sea pathways. (a) Soot-containing particles
 954 undergo heterogeneous aging processes during the transboundary transport through the
 955 inland pathway, which mainly change their mixing states from partly-coated with single
 956 soot core to embedded with single soot core structures and increase the E_{abs} change per
 957 unit D_p/D_c change at 0.6. (b) Following the transboundary transport of soot-containing
 958 particles through the sea pathway, cloud process aging becomes the dominated
 959 evolution mechanism of soot-containing particles. This process not only transforms the
 960 mixing state of soot-containing particles from partly-coated with single soot core to
 961 embedded with multiple soot core structures but also slightly enhances the E_{abs} change
 962 per unit D_p/D_c change at 0.17.